Materials Horizons



COMMUNICATION

View Article Online
View Journal | View Issue



Cite this: *Mater. Horiz.,* 2019, 6 1444

Received 25th February 2019, Accepted 1st April 2019

DOI: 10.1039/c9mh00294d

rsc.li/materials-horizons

The importance of phase equilibrium for doping efficiency: iodine doped PbTe†

James Male, Da Matthias T. Agne, Da Anuj Goyal, Dbc Shashwat Anand, Da Ian T. Witting, Da Vladan Stevanović and G. Jeffrey Snyder D *a

Semiconductor engineering relies heavily on doping efficiency and dopability. Low doping efficiency may cause low mobility and failure to reach target carrier concentrations or even the desired carrier type. Semiconducting thermoelectric materials perform best with degenerate carrier concentrations, meaning high performance in new materials might not be realized experimentally without a route to optimal doping. Doping in the classic PbTe thermoelectric system has been largely successful but reported doping efficiencies can vary, raising concerns about reproducibility. Here, we stress the importance of phase equilibria considerations during synthesis to avoid undesired intrinsic defects leading to sub-optimal doping. By saturation annealing at 973 K, we decidedly fix the composition in single crystal iodine-doped PbTe samples to be Pb-rich or Te-rich without introducing impurity phases. We show that, regardless of iodine concentration, degenerate n-type carrier concentrations with ideal doping efficiency require Pb-rich compositions. Electrons in Te-rich samples are heavily compensated by charged intrinsic Pb vacancy defects. From Hall effect measurements and a simple defect model supported by modern defect calculations, we map out the 973 K ternary Pb-Te-I phase diagram to explicitly link carrier concentration and composition. Furthermore, we discuss unintentional composition changes due to loss of volatile Te during synthesis and measurements. The methods and concepts applied here may guide doping studies on other lead chalcogenide systems as well as any doped, complex semiconductor.

Introduction

Precise control of electronic carrier concentration in semiconductor materials is foundational to microelectronics and many energy technologies. Relatively low carrier concentrations

New concepts

Defects are utilized in materials design to optimize properties of next-generation devices, including thermoelectrics, solid-state batteries, fuel cells, and photovoltaics. Semiconductors, in particular, must be doped for their many technological applications. However, the subtle effects of thermodynamics on defect concentrations and doping efficiency in semiconductors are often overlooked. This study provides a pedagogical framework to guide synthesis of high-performance semiconductors though phase equilibria considerations. It introduces a saturation annealing technique to the phase boundary mapping methodology to establish a thermodynamic pathway for the processing of precisely doped materials. Understanding connections between phase equilibrium and doping can ensure reproducible, optimal, and reliable performance in both new and classic materials systems.

 $(<10^{18}~{\rm cm}^{-3})$ are needed in transistors, diodes, and solar cells. Conversely, heavily doped semiconductors ($\sim10^{18}$ – $10^{20}~{\rm cm}^{-3}$) are typically ideal for thermoelectric devices, which can convert heat into electricity through the solid-state Seebeck effect. Carrier concentrations are typically engineered by introducing impurities known as "dopants" to achieve the desired properties. These extrinsic defects either donate electrons (if the defect is an n-type dopant) or produce holes by accepting electrons (if the defect is a p-type dopant).

A classic doped semiconductor for thermoelectric use is the PbTe system, which has a high achievable carrier concentration, or dopability, for n-type and p-type conduction.^{2–6} However, attempts to reach the ideal n-type carrier concentration are inconsistent. Some reports on the typical iodine and lanthanum dopants in PbTe require higher amounts of dopant^{7–13} than others^{5,14,15} to achieve the same carrier concentration. The observation of different doping efficiencies at seemingly identical doping levels poses serious questions about reproducibility and encourages a rigorous investigation of the effects of synthesis conditions.

Intrinsic defects that form natively in a semiconductor such as vacancies, interstitials, or antisite defects are often responsible for reducing the doping efficiency of extrinsic dopants. In

^a Department of Materials Science & Engineering, Northwestern University, Evanston, IL, USA. E-mail: jeff.snyder@northwestern.edu

b Metallurgical and Materials Engineering, Colorado School of Mines, Golden, CO, USA

^c National Renewable Energy Laboratory, Golden, CO, USA

 $[\]dagger$ Electronic supplementary information (ESI) available. See DOI: 10.1039/c9mh00294d

Communication Materials Horizons

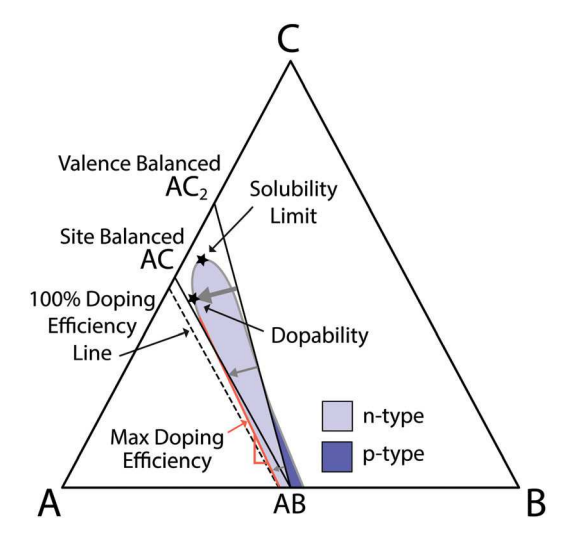


Fig. 1 A schematic, isothermal, ternary phase diagram of a binary semiconductor, AB, doped with C. The single-phase region around the compound AB has a width due to A cation and B anion vacancies and extends towards compounds AC and AC₂ due to solubility of dopant C (both width and extension are exaggerated). The single-phase region is shaded with different colors indicating n- and p-type regions. Increasing size of gray arrows corresponds to increasing n-type carrier concentration (distance from the valence balanced line between AB and AC2). The dopability (maximum n-type carrier concentration) for dopant C and the solubility limit of C are different points along the single-phase boundary. The solubility limit shows more C in the structure, but a lower carrier concentration than the dopability point due to an increased number of A cation vacancies, which form more readily with higher C content. The doping efficiency of a sample made in A-rich conditions is represented by the slope of the boundary with the single-phase region; it is not highest at the dopability or solubility points.

a self-regulating fashion resembling Le Châtelier's principle, a semiconductor tends to form charged intrinsic defects that introduce carriers of opposite charge to those added through doping. The compensation occurs because the doping reduces the formation energy of intrinsic defects with opposite charge, ^{16,17} which ultimately limits the number of carriers in the structure. Dopability, the thermodynamically achievable limit of charge carrier concentration in a semiconductor for a given dopant, is therefore determined by intrinsic defect energetics. This differs from the solubility limit of the dopant, which is the maximum concentration of dopant atoms dissolved in the solid solution. Doping efficiency, in contrast, describes the change in number of free charge carriers per dopant atom added.

The subtle differences between these doping concepts and their relations to composition can be easily visualized by considering a schematic phase diagram (Fig. 1) of a model ionic semiconductor, A²⁺B²⁻. Vacancies (either cation, A or anion B) are assumed to be the dominant defects. This is often the case, particularly for cations, which are usually smaller than the anions. Cation vacancies act as acceptor defects by failing to donate their cation electrons to the anion valence band. Their tendency to form (represented by defect formation energy) relies on the atomic chemical potentials in the system, which are synthesis dependent. As a result, the region in the phase diagram on the line between AB and B (cation-poor, anion-rich)

is p-type while the region towards A (cation-rich) is n-type. The maximum concentration of intrinsic vacancy defects is therefore related to the maximum solubility of B or A in AB. In valence compounds (*e.g.* semiconductor AB) this solubility range is often small but can never be zero – AB cannot truly be a line compound although the width in Fig. 1 is exaggerated.

Now, consider the n-type dopant, C, with valence -1 replacing B (valence -2) as a substitutional defect ($C_{\rm B}^{\bullet}$). $C_{\rm B}^{\bullet}$ donates one electron because it takes only one electron from the cations rather than the usual two per anion. Typically, such a substitutional defect is favored over vacancy defects (lower defect energy), so that the single-phase region extends more towards AC while the width towards A or B is much smaller and often drawn as a line compound (in Fig. 1 both widths are exaggerated). Any composition along the line connecting AB and AC_2 is valence balanced (e.g. $A^{2+}(C^{1-})_2$) where each addition of two C donors is compensated by removal of one A cation (creation of one A vacancy that accepts the two donated electrons). In the context of carrier doping, this line of valence balanced compositions separates the single-phase region into n- and p-type regions. In either region, carrier concentration increases with distance from the valence balanced line. Hence, the maximum number of carriers, or dopability, depends on both the amount of A (determining the vacancy content) and the amount of C in the phase. In contrast, the C solubility limit is determined solely by the maximum amount of C, giving rise to distinct dopability and solubility limit points on the phase diagram. Because valence balance and vacancy formation are energetically competing effects, one could expect the single-phase region to be pulled towards both the valence balanced and site balanced lines and end up in-between.²² The phase regions for a system dominated by antisite rather than vacancy defects (e.g. Bi₂Te₃)²³ will appear differently but similar principles apply. Further, the single-phase region will change shape with temperature due to changes in the equilibrium state (see ESI†).

While single points correspond to dopability and the solubility limit for a given dopant, it is the slope of the lines that best represent doping efficiency. For example, if the addition of C leads to 100% doping efficiency (only C_B^{\bullet} defects) there must be no additional compensating vacancy defects so the composition of A remains the same. In this case, regardless of the starting A–B composition, adding C with 100% C doping efficiency will result in compositions running parallel to the site balanced stoichiometries $(AB_{1-x}C_x)$ joining AB and AC. When doping efficiency is lower (B-rich), simultaneous formation of compensating defects leads to deviation from this slope toward the valence balanced line. Thus, doping efficiency from A- or B-rich synthesis is reflected in the slopes of the phase boundary.

Contrary to typical chemical intuition applied during synthesis, PbTe (like other "line compound" semiconductors) should have different doping properties when it is prepared slightly cation- or anion-rich. This is due to a finite width of the single-phase region near the PbTe composition^{24,25} required by configurational entropy considerations. ²⁶ It has been found both experimentally^{24,25} and theoretically²⁷ that Pb-rich PbTe is

Materials Horizons Communication

expected to have Te vacancies, each producing two electrons, while Te-rich PbTe contains Pb vacancies producing two holes each. In undoped PbTe, these intrinsic defects determine whether the material exhibits n- or p-type conduction. Similarly, we expect dopability of an extrinsic dopant such as iodine to depend heavily on the sample composition (whether Pb-rich and Te-rich) due to the different tendency to form Pb or Te vacancies.

In this study, we examine these predicted characteristics in PbTe doped with iodine to explain reports of mixed success in doping and emphasize the need for better reporting of processing conditions for reproducibility. We use a saturation annealing procedure to demonstrate the necessity of Pb-rich conditions for high n-type doping efficiency. In Te-rich conditions, iodine doped PbTe can be p-type, but n-type properties can be recovered through Pb-rich reannealing or exposure to vacuum at high temperatures. Such conditions are often inadvertently introduced through typical synthesis and/or measurement procedures. The vacancy-dominated defect model is validated by DFT and used to develop a ternary phase diagram based on the experimental carrier concentrations to visualize the relationship between doping and phase equilibria.

Experimental

The experimental phase boundary mapping methodology uses phase equilibria to precisely control composition (e.g. whether Te-rich or Pb-rich) and defect energetics in a material. It is guided by Gibbs' Phase Rule, which states that the composition of each compound in a multi-phase system is fixed at a given temperature when there are sufficient phases in equilibrium. Applying phase boundary mapping has improved thermoelectric performance in several materials, 28-33 including the recent breakthrough of n-type Mg₃Sb₂ compounds.^{21,34} Achieving well-defined phase equilibrium for this technique involves controlling sample composition to the point where secondary phases can be characterized, complicating its applicability in samples that require phase purity, such as single crystals.

Saturation annealing is a technique that can achieve the same defect control without introducing impurities. A sample near a target stoichiometry is sealed in an evacuated ampule along with some "saturating" material that consists of a mixture of phases. This effectively puts the system in equilibrium with enough phases such that Gibbs' Phase Rule does not allow compositional degrees of freedom in the sample. At a fixed pressure, the temperature of the system is the single remaining degree of freedom. The sample and saturating material (which are not in direct contact) are then equilibrated by isothermal annealing. Phase equilibrium in a system containing condensed phases (solid or liquid) requires equilibrium with the vapor at the saturated vapor pressures of the condensed phases. The chemical potential of each chemical species, i, is equal in every phase, i.e. $\mu_i^{\text{vapor}} = \mu_i^{\text{condensed}}$. Thus, in a typical saturation anneal with the sample and saturating material both in the solid phase:

$$\mu_i^{\text{sample}} = \mu_i^{\text{vapor}} = \mu_i^{\text{saturating}}$$
 (1)

and μ_i^{vapor} , which is directly related to the vapor pressure of i, will be uniquely set by the temperature. Consequently, the composition of the sample will shift during annealing to satisfy eqn (1) by exchange of vapor with the saturating material. An example saturation annealing setup for PbTe is provided in Fig. 2. Equilibrating a PbTe sample with Pb plus PbTe as the saturating material will place the system in equilibrium with Pb. As a result, the actual sample composition moves to be fixed along the Pb-rich phase boundary at the saturating temperature. This enables the same precise compositional control as phase boundary mapping methods.²¹ Saturation annealing has been successfully applied to various binary thermoelectric materials including Mg₂Si, 35,36 SnTe, 37 and Bi₂Te₃.³⁸ Similar considerations apply to the vapor phase growth of important compound semiconductors such as GaAs,³⁹ GaN,⁴⁰ and ZnO.⁴¹

Results

Saturation annealing at 973 K of undoped PbTe single crystals in Pb-rich conditions produces n-type samples, whereas p-type behavior is observed after saturation in Te-rich conditions. In both cases, the material has room temperature carrier concentrations $\sim 10^{18} \text{ cm}^{-3}$ and bipolar conduction above room temperature in agreement with previous reports. 24,25

The properties of iodine-doped PbTe also vary drastically between Pb-rich and Te-rich conditions (Table 1). Degenerate n-type behavior (>10¹⁹ cm⁻³) is measured after annealing doped samples with Pb-rich material at 973 K, while nondegenerate material is reproducibly synthesized when iodinedoped PbTe is equilibrated in Te-rich conditions. P-type conduction

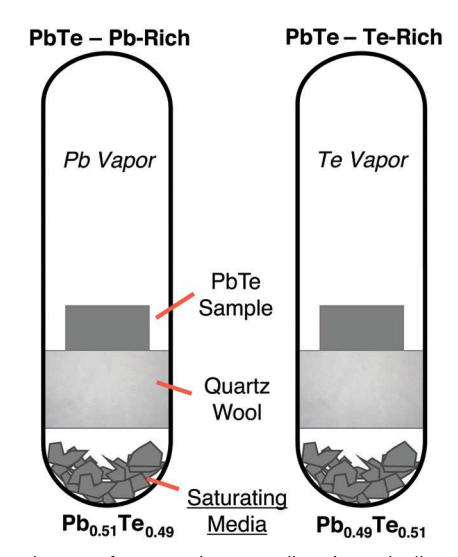


Fig. 2 Example setup for saturation annealing. A nominally stoichiometric PbTe sample is separated from a roughly equal mass of saturating material by quartz wool and sealed in a fused quartz ampule under vacuum. The saturating material is synthesized with Pb-rich or Te-rich stoichiometries and contains either Pb or Te impurities. The entire ampule is isothermally annealed at a set temperature in a tube furnace until equilibration then quenched in an ice bath.

Communication **Materials Horizons**

Table 1 Room temperature Hall carrier concentrations (n_H) measurements on nominally weighted PbTe_{1-x} I_x samples showing drastic differences after Pb- or Te-rich equilibration at 973 K. Pb-rich effective compositions (PbTe_{1-x}l_x) use 1:1 doping efficiency and Te-rich (Pb_{1-v} \square_v Te_{1-x}l_x) uses two holes per V_{Pb} to explain the measured n_{H}

Nominal composition	Effective composition (Pb-rich)	$n_{\rm H}$ (Pb-rich) (× $10^{18}~{\rm cm}^{-3}$)	Effective composition (Te-rich)	$n_{\rm H}$ (Te-rich) (× 10^{18} cm ⁻³)
$\begin{array}{c} PbTe_{0.998}I_{0.002} \\ PbTe_{0.996}I_{0.004} \\ PbTe_{0.994}I_{0.006} \end{array}$	$\begin{array}{c} PbTe_{0.99996} \square_{0.00004} \\ PbTe_{0.9978} I_{0.0022} \\ PbTe_{0.9964} I_{0.0036} \\ PbTe_{0.9953} I_{0.0047} \\ PbTe_{0.9853} I_{0.0147} \end{array}$	1.3 (n) 32 (n) 53 (n) 71 (n) 220 (n)	$\begin{array}{c} Pb_{0.9994} \square_{0.0006} Te \\ Pb_{0.9987} \square_{0.0013} Te_{0.9978} I_{0.0022} \\ Pb_{0.9981} \square_{0.0015} Te_{0.9964} I_{0.0036} \\ Pb_{0.9976} \square_{0.0024} Te_{0.9953} I_{0.0047} \\ Pb_{0.9927} \square_{0.0073} Te_{0.9853} I_{0.0147} \end{array}$	7.8 (p) 6.4 (p) 2.1 (p) 1.0 (p) 2.6 (n)

is observed at iodine concentrations < 1.47 at% of Te sites, while higher concentrations show n-type behavior (both with low effective carrier concentration).

Subsequent anneals of a single sample under both described conditions (Pb-, then Te-, then Pb-rich) shows reliable switching from n- to p- to n-type with a final carrier concentration change ~10% in both doped and undoped samples, confirming the method's validity for chemical potential control. A carrier concentration change of 10% may result from slight loss of iodine during anneals, but the magnitude of the change is near the total error of the Hall measurement.

No impurity phases are observed in powder X-ray diffraction (PXRD) patterns or energy dispersive X-ray spectroscopy (EDS) of any samples equilibrated in either condition. An example PXRD pattern is included in the ESI.† It is worth noting that it is still possible for impurities to exist in these materials below the detectable limits of the instruments used. Nevertheless, they are not expected to make significant contributions to thermoelectric properties as they are in concentrations less than ~ 2 vol%.

Fig. 3 compares Seebeck coefficient hysteresis during heating and cooling in samples nominally doped with 0.4 at% iodine to examine composition changes during a typical thermoelectric measurement. The Pb-rich sample displays degenerate n-type behavior at all measured temperatures while the Te-rich sample has intrinsic-like Seebeck coefficient behavior. Additionally, the Pb-rich sample remains degenerate and n-type after cycling between room temperature and 573 K. The Te-rich sample changes from p-type to n-type and remains n-type upon returning to room temperature, suggesting that some Te is lost.

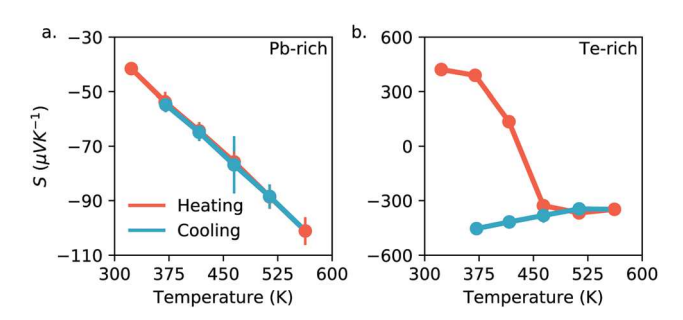


Fig. 3 Seebeck coefficient (S) of nominally doped PbTe_{0.996}I_{0.004} as a function of temperature measured over one heating/cooling cycle. (a) Saturating the sample in Pb-rich conditions results in degenerate behavior and no hysteresis. (b) An identically-doped Te-rich sample changes from p-type to n-type at moderate temperatures. Error bars in (b) are roughly represented by the size of the markers on this scale.

Seebeck measurements lasted for ~ 12 h, with the sample held at 573 K for ~ 1 h.

To validate the physical picture that emerges from experimental results and to confirm the atomistic mechanisms of iodine doping in Pb- and Te-rich PbTe, we employ modern firstprinciples defect theory and defect calculations as detailed in the Methods section.

Fig. 4a maps atomic chemical potentials representing the doped PbTe phase and the corresponding concentration (x) of iodine relative to the total Te-site concentration (1.44 imes10²² cm⁻³). Carrier concentrations calculated at 973 K across the same set of chemical potentials are shown in b, revealing p-type carrier concentrations near Te-rich compositions until x is large in agreement with experimental measurements. Defect energies calculated at the atomic chemical potentials representing Pb-rich/I-rich and Te-rich/I-rich equilibria are shown in Fig. 4c and d, respectively. The lowest energy defects at the equilibrium Fermi level $(E_{F,eq})$ at T = 973 K are expected to dominate the nature of doping in the system. In either the Pb- or Te-rich thermodynamic conditions the defect equilibrium is always between the substitutional iodine donor defect (I_{Te}^{\bullet}) and the Pb vacancy (V_{Pb}'') . In Pb-rich conditions, the V_{Pb}'' formation energy is high until the Fermi level $(E_{\rm F})$ moves deep into the conduction band, where the solubility limit of iodine would finally be reached at the $E_{F,eq}$ determined by the overall charge balance in the system (Fig. 4c). Te-rich conditions have higher I_{Te}^{\bullet} and lower V_{Pb}'' formation energies, and $E_{F,eq}$ is below the conduction band. This is a consequence of the V''_{Pb} defects accepting the electrons donated by the iodine thereby decreasing the iodine doping efficiency. Full defect plots are included in the ESI.†

Discussion

Carrier concentration measurements after saturation annealing show the necessity of ensuring Pb-rich compositions for high iodine doping efficiency and corresponding degenerate n-type behavior in PbTe. This demonstrates the importance of fixing phase equilibria - even in systems that do not have a history of pervasively difficult doping. Furthermore, the saturation annealing approach achieves phase boundary mapping without the observation of secondary impurity phases, which was previously used to confirm a sample's location in phase space.21 Rather, an impurity-free sample is "connected" to the necessary Pb or Te impurities contained in the saturating material through

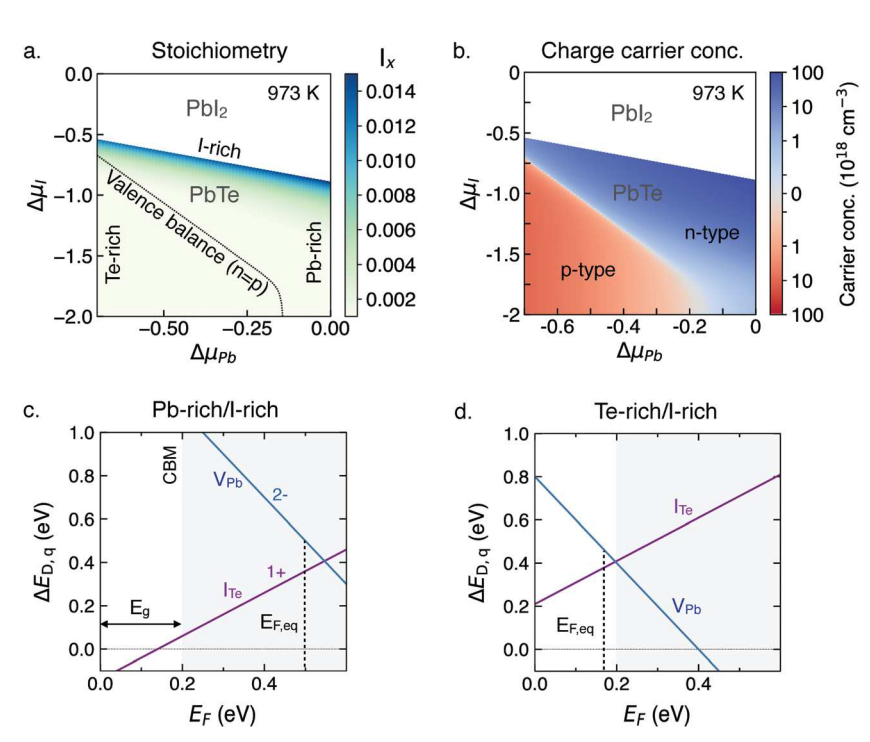


Fig. 4 (a) Pb-Te-I chemical potential space with overlaid contours representing iodine concentrations (x) on the Te site and a valence balanced line representing zero carrier concentration at 973 K. The contours in (b) represent calculated charge carrier concentrations across the same chemical potentials. (c and d) Defect formation energies calculated at chemical potentials representing (c) PbTe-Pbl₂-Pb and (d) PbTe-Pbl₂-Te equilibria. The equilibrium Fermi levels ($E_{F,eq}$) at 973 K are included in both defect plots. The gray region represents the conduction band, and the calculated band gap (E_{g}) and conduction band minimum (CBM) are labelled in (c).

the vapor phase. The vapor mediates a thermodynamic driving force that shifts the sample composition until it reaches equilibrium with a composition at the boundary of the single-phase region. While the 973 K anneals done here are above the melting points of Pb and Te, any liquid impurity forming on the sample is removed by a rough polish as evidenced by PXRD and EDS measurements, which appear single phase. Therefore, the saturation annealing method used here may prove useful in enhancing doping efficiency in single-phase samples without unwanted impurity effects.

The narrow phase width in undoped PbTe arises primarily from charged Pb or Te vacancies that can be described using Kröger-Vink notation:

$$Pb_{Pb}^{\times} \leftrightarrow Pb + V_{Pb}'' + 2h^{\bullet}$$

and

$$Te_{Te}^{\times} \leftrightarrow Te + V_{Te}^{\bullet \bullet} + 2e'$$

These are the dominant defects under Te-rich and Pb-rich conditions, respectively. The donor anti-site $Te_{Pb}^{\bullet\bullet}$ defects are ignored here for simplicity as they do not limit n-type doping in PbTe. Prior studies in this system with careful composition control show the successful donation of one electron per iodine atom in Pb-rich PbTe doped with up to 1 at% iodine. This finding aligns with the DFT defect formation energies in Fig. 4. The high calculated formation energy of $V_{Pb}^{\prime\prime}$ defects relative to I_{Te}^{\bullet} and the experimental 1:1 doping efficiency in Pb-rich conditions well below the solubility limit necessitates a negligible

 $V_{Pb}^{\prime\prime}$ concentration when the system is in equilibrium with Pb. Carrier concentrations in Pb-rich conditions are then explained by a balance between iodine donors and Te atoms on the fully occupied Te sublattice

$$Te_{Te}^{\times} + I \leftrightarrow I_{Te}^{\bullet} + e'$$

with each iodine atom in the lattice contributing one electron.

Introducing Pb vacancies in Te-rich compositions explains the intrinsic behavior by compensation of donors by V_{Pb}'' acceptors. The molar fraction, y, of V_{Pb}'' defects (\square) at a given iodine concentration, x, in $Pb_{1-y}\square_yTe_{1-x}I_x$ is explained by eqn (2) for doped samples which is used to interpret the Hall data and give the compositions reported in Table 1. Here, n_H is the measured charge carrier concentration (measured by the Hall effect) and V_m is the room temperature volume per formula unit (67.46 Å³).

$$2x - y = n_{\rm H} \times V_{\rm m} \tag{2}$$

An experimental phase diagram can be constructed (Fig. 5) for the ternary Pb–Te–I system at 973 K using compositions calculated from the defect model and an estimate of the solubility limit. The zoomed region in Fig. 5b resolves the narrow single-phase region. The stable phases surrounding PbTe are Pb, Te, and PbI₂, which are all liquid at 973 K. However, only PbTe is observed experimentally, indicating full iodine solubility at all included points. In undoped PbTe, there exists a slightly higher solubility of excess Te than of excess Pb (as inferred from the

Communication **Materials Horizons**

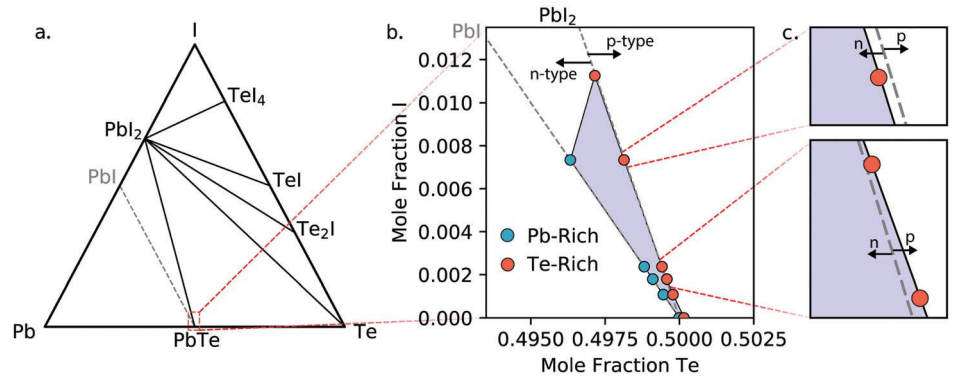


Fig. 5 (a) Ternary Pb-Te-I phase space. At 973 K, all phases surrounding PbTe are liquid. The unstable PbI phase (shown in gray) is included to indicate the site balanced line along which compositions have 100% iodine doping efficiency. (b) Magnification of the isothermal 973 K single-phase region showing experimental results. The proximity to the line connecting PbTe and PbI₂ (which represents valence balance with no carriers) emphasized in the insets (c) explains intrinsic behavior in Te-rich samples.

measured $n_{\rm H}$ – the compositional differences are too small to measure directly). The maximum solubility of iodine was established by secondary phase identification as described in the Methods.

Sample locations in Fig. 5 relative to the site balanced line connecting PbTe and PbI or valence balanced line between PbTe and PbI₂ are illustrative of doping character. Site balance on the Te site without significant V''_{Ph} defects for the Pb-rich (left) side of the phase diagram causes compositions to fall along the line between PbTe and PbI. PbI is an unstable phase at 973 K but represents the site balanced composition without V"_{Ph} (100% doping efficiency). Te-rich (right side of phase diagram) compositions lie near the valence balanced line connecting PbTe and PbI₂. The proximity of Te-rich compositions to this line explains the intrinsic (low) carrier concentrations measured in these conditions and low doping efficiency of iodine in Te-rich conditions. Compositions falling just to the right of the line are intrinsic p-type semiconductors while those on the left are slightly n-type.

The switch from p- to n-type in Te-rich $Pb_{1-y} \square_y Te_{1-x} I_x$ doesn't occur until the highest iodine doping levels ($x \sim 0.015$ and higher). For comparison, the best n-type thermoelectric performance in this system is expected at $x \sim 0.0012$ -0.0020 under Pb-rich conditions, whereas our study shows p-type conduction from Te-rich saturation at the same doping level. Clearly, there is a drastic decrease in doping efficiency and thermoelectric performance on the Te-rich side of the narrow phase width at the most relevant iodine concentrations despite minute compositional differences from the Pb-rich side.

The experimental result (Fig. 6) showing reversible crossing of the phase boundary (i.e. Pb-, then Te-, then Pb-rich) and return to nearly the same n-type carrier concentration demonstrates control of intrinsic Pb vacancies and minimal loss of iodine to the equilibrating material at 973 K. It is worth noting that greater loss of doping species through equilibration with undoped saturating material may occur with certain dopants42 and should be considered when carrying out similar

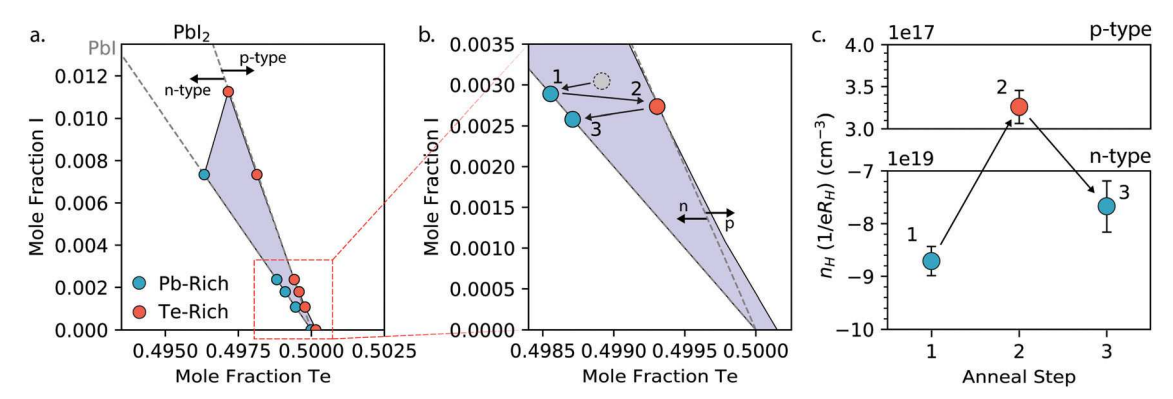


Fig. 6 (a) Magnified single-phase region from the 973 K Pb-Te-I ternary phase diagram. (b) Low dopant section of single-phase region showing experimental switching between Pb-rich and Te-rich phase boundaries. Arrows represent sequential saturation annealing steps (1. Pb-rich, 2. Te-rich, 3. Pb-rich) applied to a single sample. The gray point is a hypothetical starting point for the unsaturated sample, the exact location of which is unknown before setting the phase equilibrium. (c) Measured hall carrier concentration ($n_{\rm H}=1/(eR_{\rm H})$) at each annealing step, with negative values representing electrons and positive representing holes. Close agreement (~10%) between the two Pb-rich annealing steps demonstrates the reliability of targeting specific equilibria with this method.

experiments. In these cases, doping the saturating material to the same level as the samples should limit dopant loss.

The work undertaken here underlines the necessity of Pb-rich conditions for degenerate n-type PbTe. But, most studies do not include this requirement in their methods. This oversight may result from common experimental techniques coupled with a high Te volatility at moderate temperatures. Certain studies of n-type PbTe include a long (~48 h), hightemperature vacuum anneal for the reported purpose of improved homogeneity and mechanical strength. 5,14,15,43 Interestingly, these methods lead to doping efficiencies similar to those with Pb-rich compositions. The Seebeck coefficient hysteresis in Fig. 3b helps explain this occurrence. The p- to n-type change in the Te-rich sample over a short time at moderate temperature is indicative of Te loss or, equivalently, movement towards the Pb-rich phase boundary. Further n-type improvement might be expected from longer anneals or higher temperatures, leading to the doping efficiency observed in the studies cited above. Therefore, it is likely that compensating defects have been overlooked in this simple system because typical processes inadvertently lead to outcomes like those achieved through saturation annealing techniques.

Difficulties achieving 100% doping efficiency in n-type PbTe⁷⁻¹³ may then be attributed to slight deviations from nominally weighted PbTe compositions and subjecting samples to less total time at high temperatures, resulting in less Te loss. Fig. 7a compares $n_{\rm H}$ in this study's saturation annealed samples to literature reports on iodine-doped PbTe at increasing nominal iodine dopant levels. 7,8,11-13 These reports include a relatively small amount of high temperature processing and do not explicitly synthesize Pb-rich samples. Using the reported $n_{\rm H}$ and our defect model places these samples within the single-phase width due to electron compensation by V_{Pb}'' (Fig. 7b). Accordingly, a subtle excess of Te may unintentionally hinder doping efficiency due to introduction of compensating defects. Given the difficulty of deterministically reporting the presence of vacancies in a minute phase width, the exact effect cannot be known without phase boundary mapping methods. Thus, we emphasize the importance of reporting a sample's thermal history and steps taken to equilibrate to a given location in phase space.

Similar findings should apply to nearly all compound semiconductors. Particular attention should be paid to those with volatile components at preparation conditions. Other common semiconductor anions such as sulfur and selenium have similarly high vapor pressures as Te, e.g., other lead chalcogenides. 44-48 It is often thought that some loss of these elements occurs during measurement or material processing, but it is seldom reported or addressed beyond internal discussions. Changes in transport property measurements resulting from high temperature composition changes are expected to be important in more complicated systems as well. These can be understood by methodically exploring all accessible phase equilibria about a target composition through phase boundary mapping techniques like saturation annealing. The successful saturation anneals here demonstrate the method's versatility for fixing phase equilibria without adding impurity phases, even in single crystals.

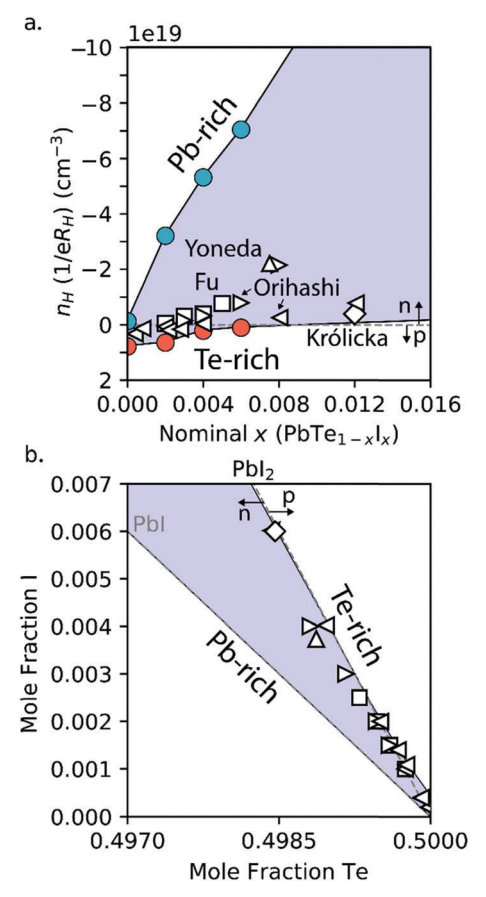


Fig. 7 (a) Measured hall carrier concentrations ($n_{\rm H}=1/(eR_{\rm H})$) for nominal x in PbTe_{1-x}I $_x$ showing high doping efficiency in Pb-rich saturation annealed samples compared to literature results. ^{7,8,11-13} Negative and positive $n_{\rm H}$ represent electron and hole concentration, respectively. (b) Compositions of literature data calculated using reported $n_{\rm H}$ and a simple defect model plotted on a low-dopant section of the Pb-Te-I ternary. Closer proximity to the valence balanced line connecting PbTe and PbI $_2$ represents lower carrier concentrations and a greater extent of charge compensation by $V_{\rm Pb}^{\rm P}$.

Conclusion

The common assumption of perfect stoichiometry in semiconductors suggests phase equilibria considerations for doping in compound semiconductors are underappreciated. We investigate phase equilibria effects on doping efficiency in the ternary Pb-Te-I system by fixing iodine-doped PbTe samples to Pb- or Te-rich compositions through a saturation annealing technique. A 973 K ternary phase diagram is drawn from Hall effect measurements and a simple defect model supported by modern, firstprinciples defect calculations following our previous work. High n-type iodine doping efficiency only occurs in Pb-rich conditions while Pb vacancies limit the electron carrier concentration in Te-rich samples. Further, we suggest that previous reports of sub-optimal doping efficiency might have been improved by loss of volatile Te in additional high temperature processing steps, emphasizing the importance of reporting annealing environment, temperatures and composition needed to define the chemical potential and phase equilibria during doped semiconductor synthesis.

Communication Methods

Defect calculations

We employ the standard supercell approach⁴⁹ using our computational framework⁵⁰ to calculate formation energies of point defects in PbTe using the following equation:

$$\Delta E_{{\rm D},q}(E_{\rm F},\mu) = \left[E_{{\rm D},q} - E_{\rm H}\right] + \sum_{i} n_i \mu_i + q E_{\rm F} + E_{\rm corr},$$
 (3)

where $\Delta E_{\mathrm{D},q}$ represents the formation energy of a point defect D in charge state q. $E_{\mathrm{D},q}$ and E_{H} are the total energies of the supercells with and without the defect, respectively. μ_i is the chemical potential of atomic species, i, describing exchange of particles with the respective reservoirs. $E_{\rm F}$ is the Fermi level and is used here to account for the possible exchange of charge between the defect and the Fermi "sea" (i.e. the charge reservoir). $E_{\rm corr}$ is a correction term to account for the finite-size corrections within the supercell approach.49 The chemical potential $\mu_i = \mu_i^0 + \Delta \mu_i$ is expressed relative to the reference elemental chemical potential, μ_i^0 , calculated using the FERE approach⁵¹ (re-fitted for HSE calculations, see ref. 27), and $\Delta \mu_i$ is the deviation from the reference elemental phase, the bounds of which are determined by the thermodynamic phase stability. Having defect formation energy allows thermodynamic modeling of defect and carrier concentrations, computed here using the approach from ref. 27 and 52. Confidence in our predictions stems from the correct description of defects and doping in our previous works, 27,50 demonstrating good agreement between calculated and measured defect and charge carrier concentrations in PbTe and other systems.

All defect calculations are performed using the VASP code, 53 employing hybrid exchange–correlation functional HSE06 54 with the exchange mixing parameter (α) equal to 0.25. The total energies of defect supercells are calculated with a plane-wave energy cutoff of 340 eV and the Brillouin zone is sampled with a G-centered Monkhorst pack k-point grid. 55 Static self-consistent spin–orbit coupling (SOC) calculations are performed on HSE relaxed defect structures. For accurate calculation of band gap and band edge energies, single-step GW calculations 56 are performed on top of HSE + SOC calculations. Further details can be found elsewhere. 27

Experimental methods

Four single crystal/large grain ingots (\sim 20 g each) of PbTe_{1-x}I_x (measured x = 0.002, 0.004. 0.008, 0.020) were synthesized from lead rod (5 N, Alfa Aesar), tellurium lump (5 N, Alfa Aesar) and lead(π) iodide granules (4N, Alfa Aesar). Nominal ratios of each element were weighed and sealed in carbon-coated fused quartz ampules under a vacuum of approximately 10^{-5} Torr. Ampules were transferred to a vertical tube furnace in which they were reacted at 1247 K, then cooled to 1122 K at a rate of 1 K h⁻¹ and held at temperature for four hours. The furnace was then switched off and samples cooled to room temperature at an uncontrolled rate. Polycrystalline Pb_{0.51}Te_{0.51} (Pb-rich) and Pb_{0.49}Te_{0.51} (Te-rich) saturation material was prepared by combining nominal masses of Pb rod (5 N, Alfa Aesar) and Te

lump (5 N, Alfa Aesar) in carbon-coated fused quartz ampules sealed under approximately 10^{-5} Torr vacuum and heating to 1273 K for at least 8 h before cold-water quenching.

Single crystal wafers (12.7 mm diameter, 1–2 mm thickness) were cut from the PbTe_{1-x}I_x ingots and saturation annealed with either Pb-rich or Te-rich saturating material under vacuum ($\sim 10^{-5}$ Torr). Equilibration was achieved by sealing each wafer in a fused quartz ampule along with an approximately equal mass of roughly crushed saturation material separated from the samples by quartz wool (see Fig. 2). These ampules were then annealed in tube furnaces at 973 K for 48 h (found to be long enough to stabilize carrier concentrations) before rapid quenching in an ice bath. Additionally, a single wafer taken from the PbTe_{0.996}I_{0.004} (nominal measured composition) ingot was annealed in Pb-rich conditions, then Te-rich conditions, then Pb-rich conditions again (Fig. 6). Hall measurements were taken after each of these equilibration steps to test reversibility.

Similarities in ionic size between Te and I and the effect of vacancy defects on the PbTe lattice parameter complicate an iodine solubility limit estimate by Vegard's Law. Tather, solubility was established through identification of secondary phases. An additional set of polycrystalline PbTe ingots were nominally doped with 2.00, 2.25, 2.50. and 2.75 at% iodine along the PbI2 line following the polycrystalline melt-quench methods described above. These allowed a rough solubility limit estimate by identifying the onset of secondary phase formation through SEM/EDS searches across relatively large ($\sim 1~\rm cm^2$) sections of the samples. The sample with the highest nominal doping level that showed no secondary phases was assumed to be near the solubility limit of iodine in PbTe.

Transport measurements were performed in-house on full wafers or large sections, with specifics of the methods described in detail elsewhere. In short, conductivity and carrier concentration were measured up to 573 K using the Van der Pauw method under a reversible magnetic field of 2 T. The Seebeck coefficient was measured to 573 K using Chromel–Nb thermocouples with an oscillating temperature gradient (max $\Delta T = 10$ K). Each sample was roughly polished before measurements.

The single crystal/large-grain ingots grown in this study can be expected to show a composition gradient along their length. Therefore, precise iodine doping levels cannot be known. An "effective" iodine doping level was obtained by assuming 1:1 doping of iodine on the Te site, which has been shown in previous work on n-type dopants in the PbTe system which utilized polycrystalline, Pb-rich samples.⁵

Phase purity was confirmed by PXRD (STOE STADI P, Cu- $K_{\alpha-1}$ radiation, step size of 0.015°) and EDS (FEI Quanta 650 ESEM with a solid-state BSE detector). An example PXRD pattern is included in the ESI.†

Conflicts of interest

The authors declare that there are no conflicts of interest related to this work.

Acknowledgements

Materials Horizons

The authors would like to thank Matthew Peters for useful discussions on the Pb-Te-I ternary phase diagram. This work is supported by the NSF DMR (DMREF) program, grant no. 1729487. Computational work is supported by NSF DMR program, grant no. 1729594, and is conducted using computational resources sponsored by the Department of Energy's Office of Energy Efficiency and Renewable Energy and located at the National Renewable Energy Laboratory. This work made use of the EPIC facility of Northwestern University's NUANCE Center, which has received support from the Soft and Hybrid Nanotechnology Experimental (SHyNE) Resource (NSF ECCS-1542205); the MRSEC program (NSF DMR-1720139) at the Materials Research Center; the International Institute for Nanotechnology (IIN); the Keck Foundation; and the State of Illinois, through the IIN. This work also made use of the IMSERC at Northwestern University, which has received support from the Soft and Hybrid Nanotechnology Experimental (SHyNE) Resource (NSF ECCS-1542205); the State of Illinois and International Institute for Nanotechnology (IIN).

References

- 1 G. J. Snyder and E. S. Toberer, *Nat. Mater.*, 2008, 7, 105–114.
- 2 J. P. Heremans, V. Jovovic, E. S. Toberer, A. Saramat, K. Kurosaki, A. Charoenphakdee, S. Yamanaka, G. J. Snyder and G. Jeffrey Snyder, *Science*, 2008, 321, 554–557.
- 3 K. Biswas, J. He, I. D. Blum, C. I. Wu, T. P. Hogan, D. N. Seidman, V. P. Dravid and M. G. Kanatzidis, *Nature*, 2012, 489, 414–418.
- 4 D. Wu, L. D. Zhao, X. Tong, W. Li, L. Wu, Q. Tan, Y. Pei, L. Huang, J. F. Li, Y. Zhu, M. G. Kanatzidis and J. He, *Energy Environ. Sci.*, 2015, 8, 2056–2068.
- 5 A. D. LaLonde, Y. Pei and G. J. Snyder, *Energy Environ. Sci.*, 2011, 4, 2090.
- 6 A. D. Lalonde, Y. Pei, H. Wang and G. Jeffrey Snyder, *Mater. Today*, 2011, **14**, 526–532.
- S. Yoneda, E. Ohta, H. T. Kaibe, I. J. Ohsugi, K. Miyamoto,
 I. A. Nishida, H. T. Kaibe, I. J. Ohsugi, K. Miyamoto,
 I. A. Nishida, H. T. Kaibe, I. J. Ohsugi, K. Miyamoto and
 I. A. Nishida, J. Cryst. Growth, 1999, 204, 229–232.
- 8 L. Fu, M. Yin, D. Wu, W. Li, D. Feng, L. Huang and J. He, Energy Environ. Sci., 2017, 10, 2030.
- 9 K. Ahn, C. Li, C. Uher and M. G. Kanatzidis, *Chem. Mater.*, 2009, **21**, 1361–1367.
- 10 G. T. Alekseeva, M. V. Vedernikov, E. A. Gurieva, P. P. Konstantinov, L. V. Prokof'eva and Y. I. Ravich, *Semiconductors*, 1998, 32, 716–719.
- 11 A. Królicka, A. Hruban, A. Materna, M. Piersa and S. Strzelecka, *Mater. Elektron.*, 2014, 42, 5–12.
- 12 M. Orihashi, Y. Noda, C. Lidong and T. Hirai, *Mater. Trans.*, 2000, 41, 1282–1286.
- 13 M. Orihashi, Y. Noda, T. H. Kaibe and I. A. Nishida, *Mater. Trans.*, 1998, **61**, 672–678.

- 14 Y. Pei, Z. M. Gibbs, A. Gloskovskii, B. Balke, W. G. Zeier and G. J. Snyder, *Adv. Energy Mater.*, 2014, 4, 1–12.
- 15 Z. M. Gibbs, A. Lalonde and G. J. Snyder, New J. Phys., 2013, 15, 075020.
- 16 A. Walsh and A. Zunger, Nat. Mater., 2017, 16, 964-967.
- 17 W. Walukiewicz, Phys. B, 2001, 302-303, 123-134.
- 18 A. Zunger, Appl. Phys. Lett., 2003, 83, 57-59.
- 19 E. S. Toberer, A. F. May and G. J. Snyder, *Chem. Mater.*, 2010, 22, 624–634.
- 20 G. S. Pomrehn, A. Zevalkink, W. G. Zeier, A. Van De Walle and G. J. Snyder, *Angew. Chem., Int. Ed.*, 2014, 53, 3422–3426.
- 21 S. Ohno, K. Imasato, S. Anand, H. Tamaki, S. D. Kang, P. Gorai, H. K. Sato, E. S. Toberer, T. Kanno and G. J. Snyder, *Joule*, 2018, 2, 141–154.
- 22 S. Anand, K. Xia, T. Zhu, C. Wolverton and G. J. Snyder, *Adv. Energy Mater.*, 2018, **8**, 1801409.
- 23 I. T. Witting, T. C. Chasapis, F. Ricci, M. Peters, N. A. Heinz, G. Hautier and G. J. Snyder, *Adv. Electron. Mater.*, DOI: 10.1002/aelm.201800904.
- 24 R. F. Brebrick and E. Gubner, *J. Chem. Phys.*, 1962, **36**, 1283–1289.
- 25 M. C. Peters, J. W. Doak, W. W. Zhang, J. E. Saal, G. B. Olson and P. W. Voorhees, *CALPHAD: Comput. Coupling Phase Diagrams Thermochem.*, 2017, 58, 17–24.
- 26 G. S. Collins, J. Mater. Sci., 2007, 42, 1915-1919.
- 27 A. Goyal, P. Gorai, E. S. Toberer and V. Stevanović, *NPJ Comput. Mater.*, 2017, 3, 42.
- 28 S. Ohno, U. Aydemir, M. Amsler, J. H. Pöhls, S. Chanakian, A. Zevalkink, M. A. White, S. K. Bux, C. Wolverton and G. J. Snyder, Adv. Funct. Mater., 2017, 27, 1606361.
- 29 B. R. Ortiz, K. Gordiz, L. C. Gomes, T. Braden, J. M. Adamczyk, J. Qu, E. Ertekin and E. Toberer, *J. Mater. Chem. A*, 2019, 7, 621–631.
- 30 C. M. Crawford, B. R. Ortiz, P. Gorai, V. Stevanovic and E. S. Toberer, *J. Mater. Chem. A*, 2018, **6**, 24175–24185.
- 31 M. Zhu, Z. Wu, Q. Liu, T.-J. Zhu, X.-B. Zhao, B. Huang, X. Tao and S.-Q. Xia, *J. Mater. Chem. A*, 2018, **6**, 11773–11782.
- 32 Y. Tang, R. Hanus, S. W. Chen and G. J. Snyder, *Nat. Commun.*, 2015, **6**, 7584.
- 33 Y. Tang, X. Li, L. H. J. Martin, E. Cuervo Reyes, T. Ivas, C. Leinenbach, S. Anand, M. Peters, G. J. Snyder and C. Battaglia, *Energy Environ. Sci.*, 2018, 11, 311–320.
- 34 P. Gorai, B. R. Ortiz, E. S. Toberer and V. Stevanović, *J. Mater. Chem. A*, 2018, **6**, 13806–13815.
- 35 D. Kato, K. Iwasaki, M. Yoshino, T. Yamada and T. Nagasaki, *Phys. Chem. Chem. Phys.*, 2018, 25939–25950.
- 36 D. Kato, K. Iwasaki, M. Yoshino, T. Yamada and T. Nagasaki, J. Solid State Chem., 2018, 258, 93–98.
- 37 H. Scherrer, S. Weber and S. Scherrer, *Phys. Lett. A*, 1980, 77, 189–190.
- 38 J. P. Fleurial, L. Gailliard, R. Triboulet, H. Scherrer and S. Scherrer, *J. Phys. Chem. Solids*, 1988, **49**, 1237–1247.
- 39 D. T. J. Hurle, J. Appl. Phys., 1999, 85, 6957-7022.
- 40 P. Boguslawski, E. L. Briggs and J. Bernholc, *Phys. Rev. B*, 1995, **51**, 17255–17258.
- 41 A. Janotti and C. G. Van De Walle, *Phys. Rev. B: Condens. Matter Mater. Phys.*, 2007, **76**, 16502.

Communication Materials Horizons

- 42 A. J. Strauss, J. Electron. Mater., 1973, 2, 553-569.
- 43 R. W. Fritts, in *Thermoelectric Materials and Devices*, ed. I. B. Cadoff and E. Miller, Reinhold Pub. Corp., New York, 1960, pp. 143–162.
- 44 H. Wang, J. Wang, X. Cao and G. J. Snyder, *J. Mater. Chem. A*, 2014, 2, 3169–3174.
- 45 H. Wang, E. Schechtel, Y. Pei and G. J. Snyder, *Adv. Energy Mater.*, 2013, 3, 488–495.
- 46 H. Wang, X. Cao, Y. Takagiwa and G. J. Snyder, *Mater. Horiz.*, 2015, **2**, 323–329.
- 47 R. F. Brebrick and E. Gubner, J. Chem. Phys., 1962, 36, 170.
- 48 R. F. Brebrick and W. W. Scanlon, *Phys. Rev.*, 1954, **96**, 598–602.
- 49 S. Lany and A. Zunger, *Modell. Simul. Mater. Sci. Eng.*, 2009, 17, 084002.
- 50 A. Goyal, G. Prashun, H. Peng, S. Lany and S. Vladan, Comput. Mater. Sci., 2017, 130, 1-9.

- 51 V. Stevanović, S. Lany, X. Zhang and A. Zunger, *Phys. Rev. B: Condens. Matter Mater. Phys.*, 2012, **85**, 115104.
- 52 K. Biswas and S. Lany, *Phys. Rev. B: Condens. Matter Mater. Phys.*, 2009, **80**, 115206.
- 53 G. Kresse and J. Furthmüller, Comput. Mater. Sci., 1996, 6, 15-50.
- 54 J. Heyd, G. E. Scuseria and M. Ernzerhof, *J. Chem. Phys.*, 2003, **118**, 8207–8215.
- 55 H. J. Monkhorst and J. D. Pack, *Phys. Rev. B*, 1976, **13**, 5188–5192.
- 56 L. Hedin, Phys. Rev., 1965, 139, 796-823.
- 57 Y. A. Ugai, M. K. Sharov and O. B. Yatsenko, *Inorg. Mater.*, 2004, **40**, 806–808.
- 58 K. A. Borup, E. S. Toberer, L. D. Zoltan, G. Nakatsukasa, M. Errico, J. P. Fleurial, B. B. Iversen and G. J. Snyder, *Rev. Sci. Instrum.*, 2012, 83, 123902.
- 59 S. Iwanaga, E. S. Toberer, A. Lalonde and G. J. Snyder, *Rev. Sci. Instrum.*, 2011, 82, 063905.